

A MICROMACHINED GEOMETRIC MOIRÉ INTERFEROMETRIC FLOATING-ELEMENT SHEAR STRESS SENSOR

S. Horowitz,^{1£} T. Chen,^{1£} V. Chandrasekaran,^{2&} K. Tedjojuwono,³
T. Nishida,^{1&} L. Cattafesta,^{2¶} and M. Sheplak^{2§}

¹Interdisciplinary Microsystems Group, Electrical & Computer Engineering, University of Florida, Gainesville, FL 32611

²Interdisciplinary Microsystems Group, Mechanical and Aerospace Engineering, P.O. Box 116250, University of Florida, Gainesville, FL 32611-6250, (352) 392-3983, FAX: (352) 392-7303, ms@mae.ufl.edu

³Advanced Measurement and Diagnostics Branch, NASA Langley Research Center, Hampton, VA 23681-2199

Abstract

This paper presents the development of a floating-element shear stress sensor that permits the direct measurement of skin friction based on geometric Moiré interferometry. The sensor was fabricated using an aligned wafer-bond/thin-back process producing optical gratings on the backside of a floating element and on the top surface of the support wafer. Experimental characterization indicates a static sensitivity of $0.26 \mu\text{m}/\text{Pa}$, a resonant frequency of 1.7 kHz , and a noise floor of $6.2 \text{ mPa}/\sqrt{\text{Hz}}$.

Introduction

The measurement of mean and fluctuating wall shear-stress in laminar, transitional, and turbulent boundary layers and channel flows has applications both in industry and the scientific community. Time-resolved, fluctuating shear-stress data can also provide physical insight into complex flow phenomena, including turbulent viscous drag, transition to turbulence, flow separation, and shock-wave/boundary layer interactions. The accurate measurement of skin friction is of vital importance to the aircraft industry. Specifically, skin friction drag

comprises roughly 50% of the total vehicle drag for a typical subsonic transport aircraft.¹ The measurement of wall shear stress also has obvious applications as an enabling technology for the emerging field of active flow control.² In biomedical applications, both mean and fluctuating wall shear stress are important hemodynamic factors in the development of arterial pathologies, such as atherosclerosis.³ Unfortunately, macro-scale measurement technology is insufficient to meet the demands of directly obtaining accurate mean and fluctuating wall shear stress data.

In his seminal review of floating-element sensors, Clauser-plot techniques, Preston tubes, obstacle methods, hot-film anemometers, mass-transfer probes, oil-film techniques, and liquid crystal methods, Winter⁴ states that, “*Of all of the techniques reviewed it is apparent that none can be considered an absolute and reliable standard.*” Fifteen years later, in another classic review article on shear stress measurement techniques, Haritonidis⁵ comes to a similar conclusion when he states, “*No doubt, improved or new instruments will soon appear that extend the rather poor or unreliable capabilities of existing instruments.*” These inadequacies are illustrated by Fernholtz et al.⁶ who reported the uncertainties in mean shear stress for surface fence methods, wall hot wires, wall pulsed wires, and oil-film interferometry to be at least 4% in incompressible flows. A recent review of point, line and image-based oil-film interferometry reported mean shear stress uncertainties of 5% for incompressible flows

£ Graduate Student, Student Member AIAA

& Associate Professor

¶ Associate Professor, Associate Fellow AIAA

§ Associate Professor, Member AIAA

Copyright © 2004 by the University of Florida. Published by the American Institute of Aeronautics and Astronautics, Inc. with permission

and 10% for supersonic flows.⁷ The same review reported liquid crystal techniques uncertainties of 5% for incompressible flows. In his review of blood flow in arteries, Ku⁸ notes that indirect methods of measurement (i.e., velocity profile measurements, hot-films, etc.) are inherently inaccurate due to a lack of knowledge of the blood viscosity at the wall and concludes, "...arterial wall shear stress measurements are estimates and may have errors of 20-50%".

Out of the listed conventional techniques, only hot-film probes and wall-mounted hot-wires offer the potential to make time-resolved, fluctuating measurements. The uncertainty of their dynamic response has not been quantified. Difficulties arise due to heat conduction, calibration difficulties, flow perturbation due to heating, and errors in response due to large fluctuations with respect to the mean (~40%).⁷ There is considerable evidence that the uncertainty of thermal sensors can be quite large in gas flow applications. In particular, a recent computational study suggests that just the flow perturbations due to heat transfer from the sensor to the flow alone can result in mean shear stress errors of 5% or greater.⁹ In addition, a single thermal sensor is unable to discern the direction of the wall shear stress which limits even their qualitative usefulness in the vicinity of separating and reattaching flows.

To accurately capture the spectrum of the turbulent shear-stress fluctuations, the measurement device must possess a large usable bandwidth, and the spatial dimensions of the device must be less than the smallest turbulent structures of interest to avoid spatial filtering. For example, at reasonably high Reynolds numbers, the spatial length scales of interest can be $O(100 \mu m)$, and the required bandwidth can be in excess of $1 kHz$.⁷ Additionally, a known, flat frequency response function is desirable for accurate turbulence spectra measurements. If time correlations are desirable, a zero phase-lag frequency response function over a wide frequency range is also desired. Therefore, the

characterization of the sensor/compensation system dynamic response is necessary to bound measurement uncertainty. In summary, the accurate, direct measurement of fluctuating wall shear stress has not been realized via conventional measurement technology. As will be shown below, the inherent characteristics of microfabricated transducers offer the potential to realize these measurements.

Microelectromechanical systems (MEMS) technology extends silicon-based integrated circuit (IC), microfabrication technology to manufacture miniature engineering systems.¹⁰ Micromachining technology provides the opportunity to synthesize transducers possessing superior performance compared to mainstream mechanical fabrication techniques. Specifically, the small physical size and corresponding reduced mass of micro-sensors offers the potential to vastly improve both the temporal and spatial measurement bandwidth.

Realizing the potential advantages of miniaturization scaling, the MEMS community has developed both thermal,^{11,12} floating element,¹³⁻¹⁸ and optical shear-stress sensors. Thermal sensors are robust and simpler to fabricate; however, they are based on a heat transfer analogy and absolute calibration for quantitative measurements is difficult.⁷ Optical MEMS (MOEMS)-based laser-Doppler anemometers that measures velocity gradient in the viscous sublayer are very promising, but the ability to generate a sufficiently small measurement volume in a high-Reynolds number sublayer is challenging.¹⁹ Conversely, floating-element structures provide the best opportunity to obtain direct quantitative, time-resolved measurements in a controlled wind tunnel environment. Several transduction techniques exist for measurement of the shear-stress induced deflection of the floating element, including capacitive,^{13,14,18} piezoresistive,^{15,16} and differential optical shutter techniques.¹⁷ An ideal sensor is truly flush-mounted with no wire bonds that generate flow disturbances and is immune to non-shear stress inputs (i.e., electromagnetic interference (EMI), pressure

fluctuations, etc.). Only one existing device does not possess front-side wire-bonds, but it was not designed for turbulence applications and possesses too low a sensitivity.¹⁶ The optical shutter technique¹⁷ provided immunity to EMI and pressure fluctuations, but it possessed wire bonds and was sensitive to tunnel vibration due to the separation of the light source from the sensor. Addition information comparing these devices is given by Naughton and Sheplak⁷ in their review of MEMS-based shear stress sensors.

We have attempted to address the limitations of existing MEMS shear stress sensor technology via the development of a floating-element shear stress sensor that permits the direct measurement of skin friction based on geometric Moiré interferometry. The next section describes the mechanical design of the floating element and reviews geometric Moiré interferometry to deflection transduction. This is followed by a discussion of the device microfabrication. The experimental methods and results of the experimental characterization are then given. Finally, this paper is concluded and suggestions for future work are given.

Shear Stress Sensor Design

Floating-element sensors directly measure the integrated force produced by the wall shear stress on a flush-mounted movable “floating” element. The floating element is attached to either a displacement transducer or is part of a feedback force-rebalance configuration. For our sensor, the displacement transducer consists of optical gratings on the backside of a floating element and on the top surface of the support wafer that superimpose to form a Moiré fringe which amplifies the element translation. This section presents a first-order mechanical model of the floating element and introduces geometric Moiré interferometry. It concludes with the sensor device structure and the microfabrication process.

A schematic of a generic MEMS floating element structure is given in Figure 1. The floating element possesses a length, L_e , width

W_e and thickness t . The floating element is suspended over a recessed gap g by silicon tethers that also serve as restoring springs. The displacement δ of the floating element as a function of wall shear stress, τ_w , is determined via Euler-Bernoulli beam theory to be

$$\delta = \tau_w \frac{L_e W_e}{4Et} \left(\frac{L_t}{W_t} \right)^3 \left\{ 1 + 2 \frac{L_t W_t}{L_e W_e} \right\}, \quad (1)$$

where L_t is the tether length, W_t is the tether width, and E is the elastic modulus of the tether.¹³ Euler-Bernoulli beam theory assumes small deflections such that the strain at the neutral axis of the beam can be neglected. For sufficiently large shear stresses applied to a device, this theory will fail. The limits of this approximation can be approximated via a large-deflection energy-based solution,

$$\delta \left[1 + \left(\frac{3}{4} \right) \left(\frac{\delta}{W_t} \right)^2 \right] = \frac{\tau_w W_e L_e}{4Et} \left[\frac{L_t}{W_t} \right]^3 \left[1 + 2 \frac{W_t L_t}{W_e L_e} \right] \quad (2)$$

From Eq. (2), it is clear that the maximum deflection of the floating element must be a fraction of the tether width for the small deflection solution given in Eq. (1) to be valid.

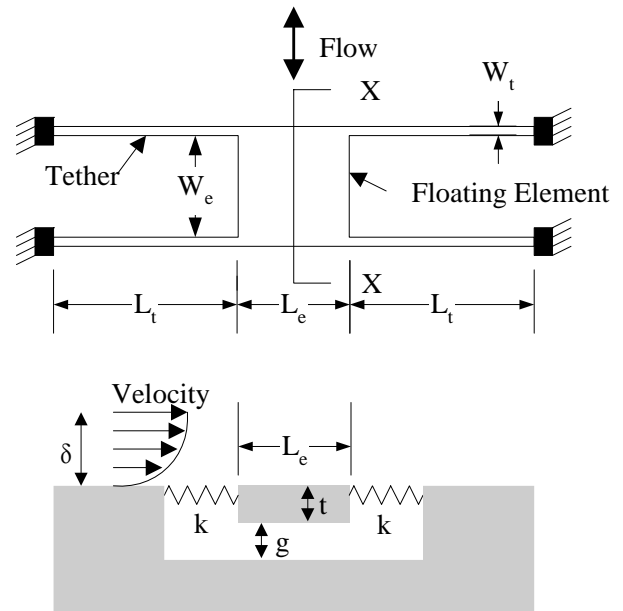


Figure 1: Schematic plan view and cross-section of a typical floating-element sensor.

The element possesses an effective mass, M , and the tethers possess an effective spring constant, k . The mechanical sensitivity of the sensor with respect to the integrated shear stress force, $F_\tau = \tau_w W_e L_e$, is directly proportional to the compliance of the tethers, $1/k$

$$\frac{1}{k} = \frac{\delta}{F_\tau} = \frac{1}{4Et} \left(\frac{L_t}{W_t} \right)^3 \left\{ 1 + 2 \frac{L_t W_t}{L_e W_e} \right\} \quad (3)$$

The compliance of the device will be limited either by failure at the maximum applied shear stress or from the onset of geometric nonlinearities in the force-displacement relationship shown in Eq. (2). The requirement of high spatial resolution requires the measurement of very small forces. For example, a sensor possessing a $100 \mu\text{m}^2$ floating element structure would need to measure a 10 pN force to resolve a shear stress level of 1 mPa , thus requiring a highly compliant structure. If $L_e W_e \gg L_t W_t$, then the effective mass is approximated by $M \approx \rho L_e W_e t$, where ρ is the mass-averaged density of the element material. Assuming a perfectly-damped or under-damped system, the bandwidth is proportional to the first resonance of the device, $\sqrt{k/M}$. Therefore, the shear-stress sensitivity-bandwidth product for the device is proportional to

$$\frac{1}{\sqrt{kM}} \propto \sqrt{\frac{1}{4E\rho L_e W_e t^2} \left(\frac{L_t}{W_t} \right)^3}. \quad (4)$$

The sensitivity-bandwidth product is a useful figure of merit to investigate the scaling of mechanical sensors analogous to the gain-bandwidth product of an operational amplifier. This figure of merit illustrates that MEMS technology enables the development of low mass, compliant mechanical sensors possessing superior sensitivity-bandwidth products relative to conventional sensors. As is the case in all transducers, the minimum detectable signal will be determined by the electronic and/or thermal-mechanical noise floor of the measurement

system.²⁰ The favorable miniaturization scaling of the mechanics of the structure is somewhat mitigated by the requirement to measure very small displacements that can be $O(\text{\AA})$.¹⁷

Our device structure consists of a $1280 \mu\text{m} \times 400 \mu\text{m}$ silicon floating element of $10 \mu\text{m}$ thickness, suspended $2.0 \mu\text{m}$ above the surface of a $500 \mu\text{m}$ thick Pyrex wafer by four $545 \mu\text{m} \times 6 \mu\text{m}$ tethers of $10 \mu\text{m}$ thickness (Figure 2). The Moiré pattern is realized by patterning aluminum lines with a different pitch on both the bottom of the floating element, g_2 , and on the Pyrex wafer, g_1 . When the device is illuminated through the floating element, light is transmitted by the superposed top and bottom gratings, creating a translation-dependent Moiré fringe pattern.

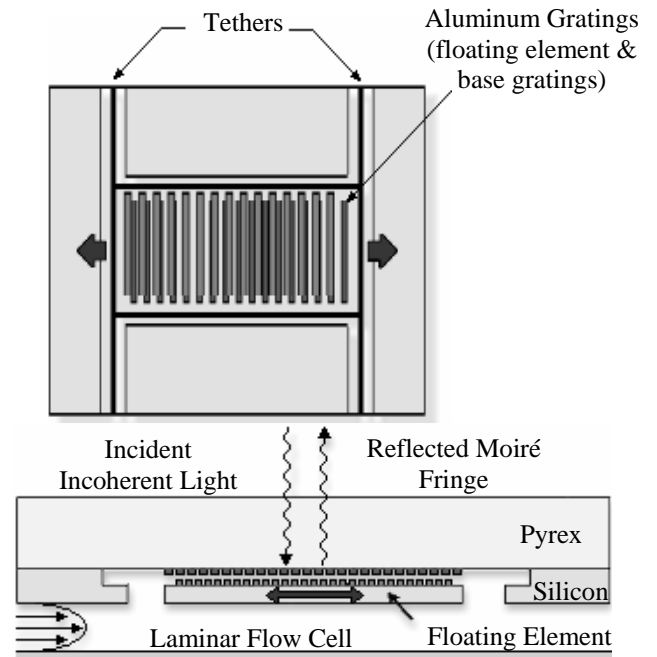


Figure 2: Top view and cross sectional schematic of the first-generation optical shear-stress sensor. Note: drawings not to scale.

A Moiré fringe pattern occurs when two gratings of almost identical spatial period are superimposed as shown in

Figure 3. The Moiré fringe pitch, G , is related to the individual grating pitches, g_1 and g_2 by²¹

$$\frac{1}{g_1} - \frac{1}{g_2} = \frac{1}{G}. \quad (5)$$

The Moiré fringe shift amplifies small displacements by the ratio of the fringe pitch, G , to the movable grating pitch, g_2 , and is invariant to intensity modulations.²¹ The displacement Δ of the Moiré fringe is

$$\Delta = \delta \left(\frac{G}{g_2} \right), \quad (6)$$

where δ is the physical displacement of the floating element displacement. The Moiré fringe displacement is therefore amplified over the grating displacement by a factor of G/g_2 . For the device presented in this paper, $g_1=9.9 \mu\text{m}$, $g_2=10 \mu\text{m}$, and $G=990 \mu\text{m}$.

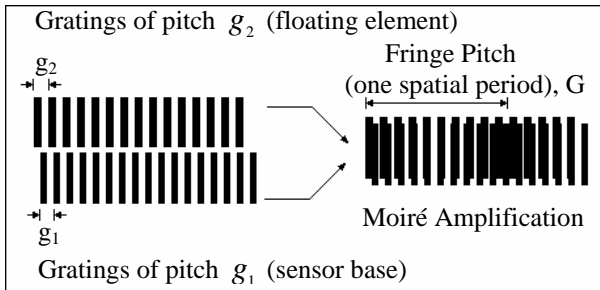


Figure 3: Geometric Moiré pattern generated from two gratings where $g_1=9.9 \mu\text{m}$, $g_2=10 \mu\text{m}$, and $G=990 \mu\text{m}$.

The sensor was fabricated using an aligned SOI/Pyrex anodic bond, thin-back process that is schematically outlined in Figure 4. A top view of the final fabricated device is shown in Figure 5.

Experimental Procedure

The experiments were performed in the Interdisciplinary Microsystems Laboratory at the University of Florida. The characterization of the shear-stress sensor included static and dynamic calibrations as well as the determination of the device noise floor.

Static Calibration Setup

Prior to testing, the sensor was packaged by inserting the die flush-mounted in a Lucite plug with front-side imaging optics and a Thomson-CSF TH78CE13 linescan CCD camera. The CCD camera contains an array of 1×1024 pixels, each $10 \mu\text{m}$ in width. The packaged device was then mounted into a $100 \text{ mm} \times 1 \text{ mm}$ flow cell that provides a variable mean shear stress (Figure 6) via a laminar, incompressible, fully developed, 2-D pressure driven flow in a slot.¹²

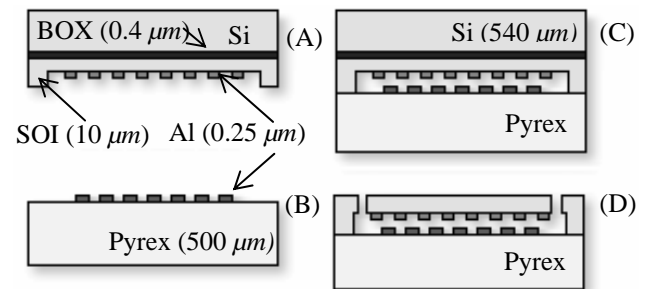


Figure 4: A schematic of the fabrication sequence: (A) Etch $2 \mu\text{m}$ recess in Si-overlayer of SOI wafers, then deposit and pattern device gratings ($0.25 \mu\text{m}$ - Al). (B) Deposit and pattern handle gratings on the Pyrex wafer ($0.25 \mu\text{m}$ - Al) (C) Align, then anodic bond the Pyrex and SOI wafers. (D) Thin-back the bulk of the SOI wafer using KOH, stopping on BOX, then use DRIE to release the floating element and tethers. Note: schematics not to scale.

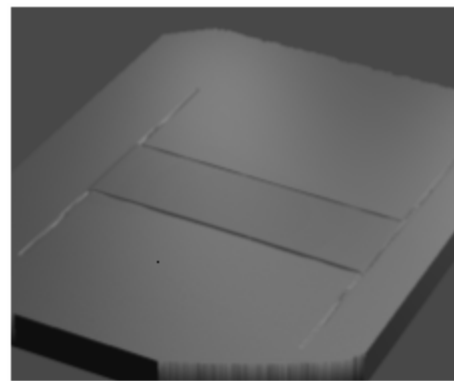


Figure 5: Top-view of the floating element shear stress sensor using an optical profilometer.

A block diagram of the static calibration procedure is given in Figure 7. A mass flow controller is used to provide a steady flow of air through a laminar flow cell, and is controlled by a PC via a Keithley 2000 Sourcemeeter. The

differential pressure between two locations in the fully-developed region of the laminar flow cell is measured via a Heise pressure sensor, which is then used to compute the applied shear stress to the sensor. This differential pressure measurement is averaged 100 times and used to compute the applied shear stress via

$$\tau_w = -\frac{h \Delta p}{2 L}, \quad (7)$$

where Δp is the differential pressure, h is the height of the channel, and L is the distance separating the pressure ports.

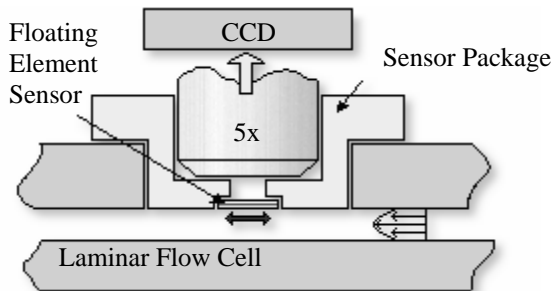


Figure 6: Schematic diagram of static calibration experimental setup illustrating backside imaging optics for 2-D laminar flow cell.

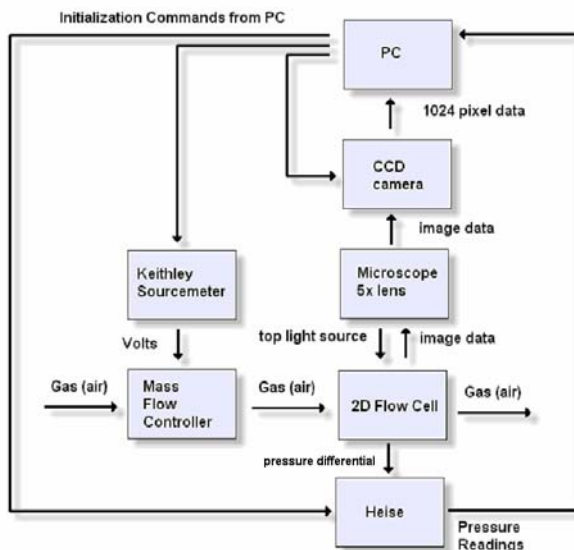


Figure 7: Schematic diagram of experimental setup for static calibration.

The Moiré fringe pattern is captured using the CCD camera coupled to a 5x optical lens. The capture process is repeated 600 times to

obtain an average fringe pattern for a no-flow or zero shear stress case. The resulting intensity pattern is normalized by a calibration image to eliminate pixel gain variations and non-uniform illumination effects. A Fast-Fourier Transform (FFT) is performed on the averaged fringe pattern. The phase of the Moiré pattern is then extracted from the FFT at the frequency corresponding to the Moiré pitch. This phase is then used as the zero reference point for determining the phase shift at an applied level of shear stress. The procedure is then repeated for a given applied shear stress and the corresponding intensity pattern to obtain the phase shift and, hence, the pixel shift. Using knowledge of the Moiré pattern and optical magnification, the corresponding mechanical displacement of the floating element is computed to give a direct measurement of the wall shear stress.

Dynamic Calibration Setup

Dynamic calibration was performed using acoustic excitation of shear-stress in a plane-wave tube. This technique utilizes acoustic plane waves in a duct to generate known oscillating wall shear stresses.²² The basic principle of this technique relies on the fact that the particle velocity of the acoustic waves is zero at the wall due to the no-slip boundary condition. This leads to the generation of a frequency-dependent boundary layer thickness and a corresponding wall shear stress. Specifically, the linearized compressible momentum equation in the axial direction reduces to the classic problem of a duct flow driven by an oscillatory pressure gradient. Therefore, at a given location, the relationship between the fluctuating shear stress and acoustic pressure is known theoretically. A conceptual schematic of the dynamical calibration setup is shown in Figure 8. A function generator is used to generate a known sinusoidal input that is then amplified and routed to a JBL 2426H speaker mounted to the end of the plane wave tube. The shear stress sensor is flush mounted to the wall of the plane wave tube directly across from a

Brüel & Kjør 4138 1/8" microphone. The CCD camera and frame grabber from the static calibration setup are used to record an image of the shear stress sensor. In the dynamic calibration, however, the camera is programmed to record 16,384 lines at a line rate of 11.42 kHz. The microphone signal is routed through a SRS-560 preamplifier to provide AC coupling and recorded by a DAQ card. The DAQ card is programmed to sample at the same linescan rate as the camera and is triggered by a synchronization pulse from the camera to provide simultaneous sampling of the microphone and shear stress signals.

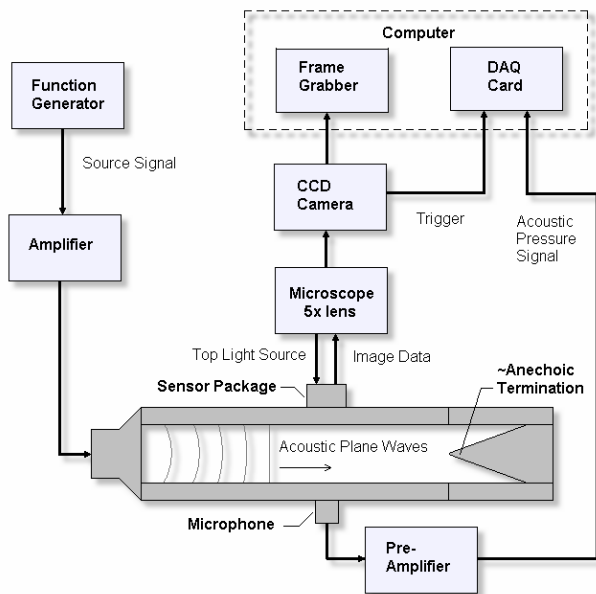


Figure 8: Schematic diagram of experimental setup for dynamic calibration.

Results and Discussion

Static Calibration Results

The recorded Moiré intensity pattern for a shear stress of 0 Pa is shown in grayscale in Figure 9, and the fringe pattern for shear stresses of 0 Pa and 1.3 Pa are shown vs. pixel number in Figure 10. The peak in relative intensity corresponds to brightest in the grayscale image. The Moiré pattern was found to have a spatial period of 1002 μm, before the 5x optical amplification, compared to the

physical grating period of 9.9 μm. The Moiré amplification for the sensor was then found to be 101.2 compared to our designed value of $G/g_2 = 99$.

Following the procedure outlined above, the pixel shift of the Moiré fringe pattern was determined for a range of applied shear-stress. The results are shown in Figure 11, along with the corresponding mechanical displacement. The mechanical sensitivity, as found from the slope of this curve, is 0.26 μm/Pa, while the Moiré fringe, after the 5x optical amplification, moves by 130.02 μm/Pa.

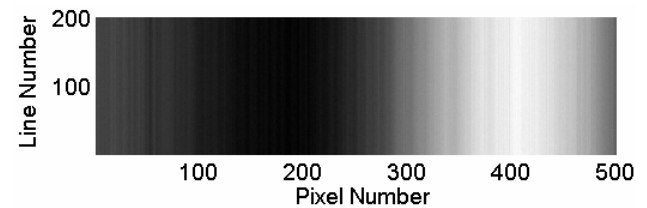


Figure 9: Moiré fringe pattern for shear stress of 0 Pa as seen by 1024 pixel linescan camera. Successive frames from the camera are stacked vertically.

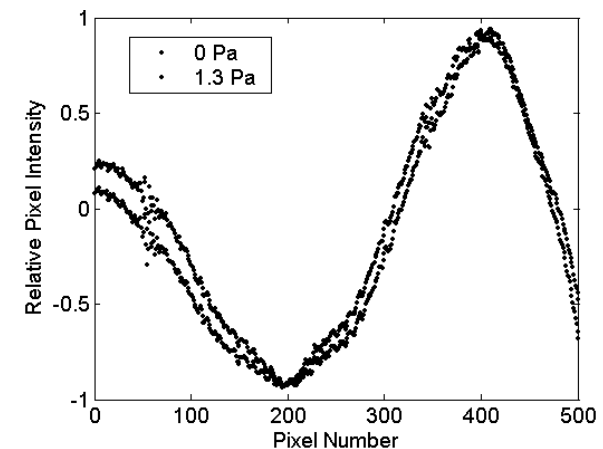


Figure 10: Measured relative pixel intensity overlaid with least squares curve fit for 0 Pa and 1.3 Pa of shear stress.

The recessed gap under the floating element gives rise to pressure-gradient induced errors. The magnitude of the effective shear-stress, τ_{eff} , acting in the presence of a pressure gradient has been shown to be

$$\tau_{eff} = \left(1 + \frac{g}{h} + \frac{2t}{h}\right) \tau_w \quad (8)$$

where h is the channel height of the wind tunnel used for calibration, g is the recessed gap, and τ_w is the actual wall shear stress.¹³ The second and third terms in the bracket are the error terms associated with flow under the floating element and the pressure gradient acting on the lip of the element, respectively. For the current device and experimental apparatus, this component of the calibration error is 2%.

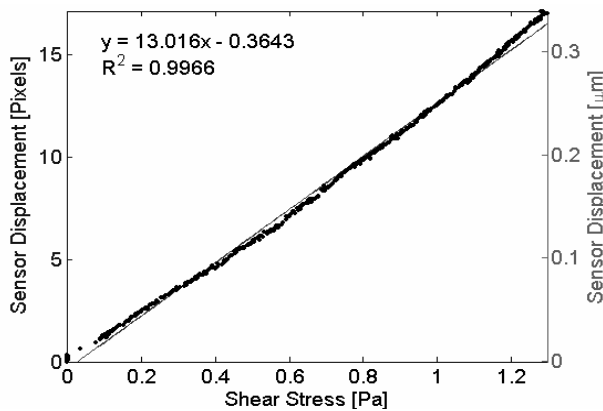


Figure 11: Static response of the sensor in terms of Moiré fringe pixel displacement and corresponding mechanical displacement as a function of mean shear stress. The static sensitivities are 13.0 pixels/Pa and 0.26 $\mu\text{m}/\text{Pa}$.

Dynamic Calibration Results

Figure 12 shows a “stacked” Moiré fringe pattern image of 40 successive line scans resulting from a sinusoidal shear stress of amplitude 0.061 Pa and frequency of 1 kHz. Successive lines from the camera are stacked vertically illustrating the oscillatory fringe pattern. The sinusoidal time trace on the right represents the input oscillatory shear stress. The data reduction procedure outlined above is used to compute the instantaneous sensor displacement for each line. Time series data illustrating the dynamic response of the sensor in terms of Moiré fringe pixel displacement and corresponding mechanical displacement for a 1 kHz sinusoidal input of 0.061 Pa is shown in Figure 13. The amplitude of the sensor displacement is approximately 3 pixels or 0.06 μm .

A preliminary estimate of the frequency response function gain factor is shown in

Figure 14 indicates a first lateral mode resonant frequency at 1.7 kHz. The corresponding phase has not been accurately estimated due to synchronization issues between the linescan CCD and the microphone channel’s analog-to-digital converter. This issue arose despite the trigger signal from the CCD camera that is used to trigger the start of microphone sampling. It is believed that round-off error in the sampling rate of the DAQ card leads to a gradual loss of synchronization over time. Further work is necessary to elucidate the precise nature of this issue.

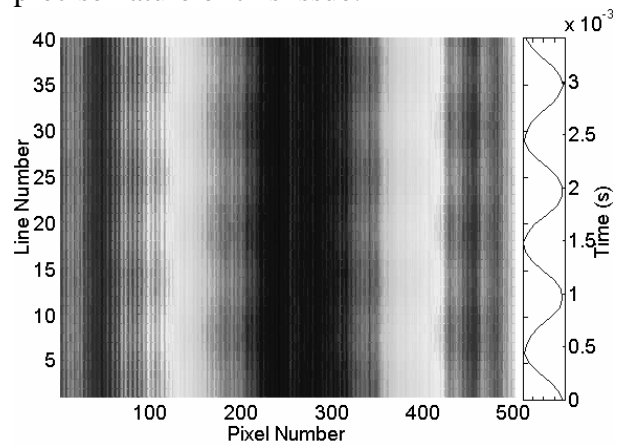


Figure 12: Moiré fringe pattern for a sinusoidal shear stress of amplitude 0.061 Pa and frequency of 1 kHz. Note: image has been modified to emphasize oscillations.

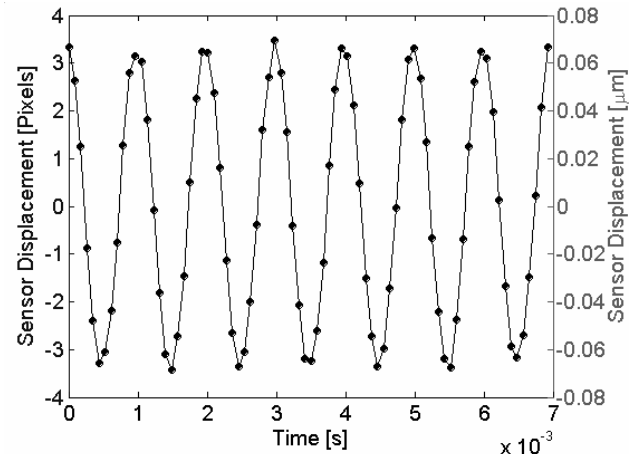


Figure 13: Time-domain waveform of Moiré shift in terms of CCD camera pixels for a sinusoidal shear stress of amplitude 0.061 Pa and frequency of 1 kHz. The dots are the actual samples taken and the line is a curve fit to the data.

The dynamic range of the sensor is ultimately limited by the device noise floor. The noise floor spectrum was obtained by recording microphone and CCD data with no acoustic input signal. An estimate of the noise floor magnitude in is shown in Figure 15. For a 1 Hz bin centered at 1 kHz, the noise floor is 1.6 nm/ $\sqrt{\text{Hz}}$ or 0.08 pixels/ $\sqrt{\text{Hz}}$, which corresponds to a minimum detectable shear stress of 6.2 mPa/ $\sqrt{\text{Hz}}$.

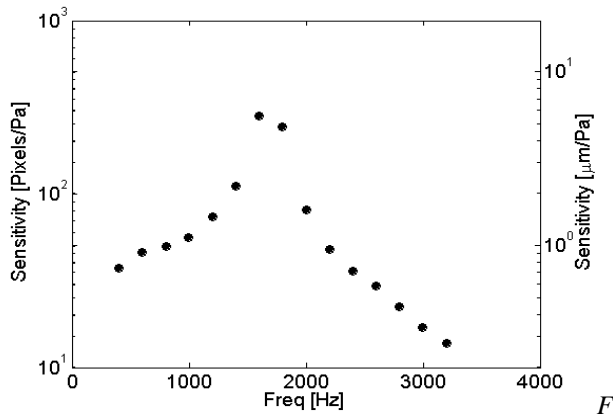


Figure 14: Magnitude of normalized frequency response function

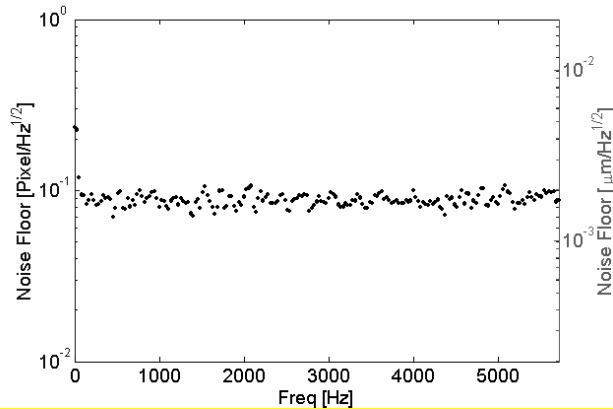


Figure 15: Noise floor spectrum of sensor with a 1 Hz binwidth. For a 1 Hz bin centered at 1 kHz, the noise floor is 1.6 nm/ $\sqrt{\text{Hz}}$ which corresponds to a minimum detectable shear stress of 6.2 mPa/ $\sqrt{\text{Hz}}$.

Conclusions

A proof-of-concept micromachined, floating element shear-stress sensor was developed that utilizes a geometric Moiré interferometric technique. A static characterization of the device revealed a linear response up to 1.3 Pa.

Noise floor measurements indicate a minimum detectable shear stress of 6.2 mPa. Therefore, the experimentally determined dynamic range is 6.2 mPa – 1.3 Pa. The upper end of the dynamic range as predicted by Eq. (2) for a 3% static non-linearity is 21.7 Pa. This, however, could not be verified due to constraints in our static calibration apparatus.

In the dynamic experiments, the device exhibited a lower resonant frequency than was expected; however it is believed to be due to a layer of photoresist that was not removed prior to testing. In addition, fabrication-induced geometric errors have not yet been quantified.

Future work will include more rigorous dynamic and static characterization, noise floor studies, and sensitivity to non-shear stress inputs, as well as resolving the dynamic calibration synchronization issue. In addition, a boroscope based imaging system will be implemented to reduce package size and improve portability. A second-generation device is planned in which the sensor geometry and Moiré fringe design will be optimized.

Acknowledgements

The authors would like to thank Professor Peter Ifju, Hamed Kourouma, Johanna Peña and Julio Castro for their assistance in this project. This work was supported through NASA-LaRC grant NAG-1-2133 and NASA-KSC grant NAG-10-316.

References

1. Hefner, J.N. and Bushnell, D.M., “An Overview of Concepts for Aircraft Drag Reduction,” *AGARD-R-654*, 1977.
2. Gad-el-Hak, M., “Flow Control: The Future,” *AIAA J. of Aircraft*, Vol. 38, No. 3, pp. 402-418, May-June 2001.
3. Grigioni, M. Daniele, C., D’Avenio, G., and Pontrelli, G., “The Role of Wall Shear Stress in Unsteady Vascular Dynamics,” *Progress in Biomedical Research*, Vol. 7, No. 3, 2002, pp. 204-212.

4. Winter, K.G., "An Outline of the Techniques Available for the Measurement of Skin Friction in Turbulent Boundary Layers," *Progress in the Aeronautical Sciences*, Vol. 18, 1977, pp. 1-57.
5. Haritonidis, J.H., "The Measurement of Wall Shear Stress," *Advances in Fluid Mechanics Measurements*, Ed. by M. Gad-El-Hak, Springer-Verlag, 1989, pp. 229-261.
6. Fernholtz, H.H., Janke, G., Schober, M., Wagner, P.M., and Warnack, D., "New Developments and Applications of Skin-Friction Measuring Techniques" *Meas. Sci. Technol.*, Vol. 7, 1996, pp. 1396-1409.
7. Naughton, J. and Sheplak, M., "Modern Developments in Shear-Stress Measurement," *Prog. Aero. Sci.*, Vol. 38, 515-570, (2002).
8. Ku, D.N., "Blood Flow in Arteries," *Annu. Rev. Fluid Mech.*, Vol. 29, 1997, pp. 299-434.
9. Appukuttan, A., Shyy, W., Sheplak, M., and Cattafesta, L., "Mixed Convection Induced by MEMS-Based Thermal Shear Stress Sensors," *Numerical Heat Transfer-A*, Vol. 43, No. 3, 2003, pp. 283-305
10. Madou, M., Fundamentals of Microfabrication, CRC Press, New York, 1997.
11. Liu C, Huang C-B, Zhu Z, Jiang F, Tung S, Tai Y-C, and Ho C-M., "A Micromachined Flow Shear-Stress Sensor Based on Thermal Transfer Principles," *J. MEMS*, Vol. 8, pp. 90-99, (1999).
12. Sheplak M, Chandrasekaran V, Cain A, Nishida T, Cattafesta L. , "Characterization of a Micromachined Thermal Shear Stress Sensor," *AIAA J*, Vol. 40, No. 6, pp. 1099-1104, (2002).
13. Schmidt MA, Howe RT, Senturia SD, Haritonidis JH, "Design and Calibration of a Microfabricated Floating-Element Shear-Stress Sensor," *Trans. Electron Dev.*, ED-35, pp. 750-757, (1988).
14. Pan, T, Hyman D, Mehregany M, Reshotko E, Garverick S, Microfabricated Shear Stress Sensors, Part 1: Design and Fabrication," *AIAA J*, Vol. 37, pp. 66-72, (1999).
15. Ng K, Shajji J, Schmidt MA, "A Liquid Shear-Stress Sensor Using Wafer-Bonding Technology," *J. MEMS* Vol. 1, pp. 89-94, (1992).
16. Goldberg HD, Breuer KS, Schmidt MA, "A Silicon Wafer-Bonding Technology for Microfabricated Shear-Stress Sensors with Backside Contacts," *Tech. Dig., Solid-State Sensor and Actuator Workshop*, pp. 111-115, (1994).
17. Padmanabhan A, Goldberg HD, Schmidt MA, Breuer KS, "A Wafer-Bonded Floating-Element Shear-Stress Microsensor with Optical Position Sensing by Photodiodes," *J. MEMS*, 5, 307-315, (1996).
18. Zhe, J, Farmer, K.R., and Modi, V., "A MEMS Device for Measurement of Skin Friction Using Capacitance Sensing," *Proc. of IEEE MEMS 01*, pp. 4-7, (2001).
19. Fourquette, D., Modarress, D., Taugwalder, F, Wilson, D., Koochesfahani, M, and Gharib, M., "Miniature and MOEMS Flow Sensors," AIAA Paper 2001-2982, 2001.
20. Gabrielson, T., B., "Mechanical-Thermal Noise in Micromachined Acoustic and Vibration Sensors," *IEEE Electron Devices*, 40, 1993, pp. 903-909.
21. Post D, Han B, and Ifju P, High Sensitivity Moiré: Experimental Analysis for Mechanics and Materials, Springer, NY, Chap. 3, 1994.
22. Sheplak, M., Padmanabhan, A., Schmidt, M.A., and Breuer, K.S., "Dynamic Calibration of a Shear Stress Sensor using Stokes Layer Excitation," *AIAA Journal*, Vol. 39, No.5, pp. 819-823, 2001.